PROCEEDINGS, 41st Workshop on Geothermal Reservoir Engineering
Stanford University, Stanford, California, February 22-24, 2016
SGP-TR-209

Toward the Construction of a 3D Velocity Model for Raft River Geothermal Field Using Ambient Noise

Xiaoning Yang[1], Lianjie Huang[1], Ileana Tibuleac[2], Ernest Majer[3], Katie Freeman[3] and Steve Jarpe[4]

[1]Los Alamos National Laboratory, B. O. Box 1663, Los Alamos, NM 87545

[2]University of Nevada, Reno, 1664 N Virginia Street, Reno, NV 89557

[3]Lawrence Berkeley National Laboratory, One Cyclotron Road, Berkeley, CA 94720

[4]Jarpe Data Solutions, 4113 N. LA Jolla Dr., Prescott Valley, AZ 86314

Corresponding Author E-mail: xyang@lanl.gov

Keywords: Ambient Seismic Noise, 3D Velocity Model

ABSTRACT

Ambient seismic noise from a geothermal field can provide useful initial information for high-resolution velocity model building. We extract fundamental-mode Rayleigh wave dispersion from seismic ambient noise and invert these travel times for a 3D velocity model for the Raft River geothermal field. We calculate cross correlations (CC) of ambient noise data recorded by eight geophones distributed in the geothermal field. To measure the surface-wave dispersion from the Green's Functions (GF) that emerge from the noise CC, we perform Multiple Filter Analysis (MFA) of the CC. Rayleigh-wave dispersion is measured between 0.2 and 35 Hz. Using measured surface-wave dispersion, we conduct tomographic inversions to construct 2D surface-wave velocity models at multiple frequencies. We are able to achieve a model resolution of several hundred meters and a travel-time misfit reduction of larger than 80% at certain frequencies. These 2D surface-wave travel-time models could be used to construct a 3D velocity model of the Raft River geothermal field through 1D inversion of surface-wave dispersion at model-node locations. The resulting 3D velocity model could serve as the first-stage, low-resolution background model in a multi-scale model building effort to construct a high-fidelity and high-resolution 3D velocity model for subsurface imaging and micro-earthquake location and focal mechanism inversions.

1. INTRODUCTION

Developing high-fidelity and high-resolution 3D velocity models for geothermal fields is important for underground fluid-flow monitoring and micro-seismicity characterization. Traditionally, these models were constructed from active-survey data alone. To better constrain the model, we would combine both active and passive seismic data to develop a 3D velocity model for an Enhanced Geothermal System (EGS) project at the Raft River geothermal field. This study focuses on the exploitation of ambient seismic noise to build an initial, low-resolution model using surface waves. The initial model serves as the initial model in velocity inversions with active seismic data and data from local earthquakes to improve resolution and reduce uncertainty of velocity models.

Using ambient seismic noise as a tool to investigate material properties of the Earth structure has become a mature technique. This is particularly true for large-scale Earth model inversions using low-frequency (< 0.15Hz) ambient seismic noise generated mainly by oceans. In the last few years, seismologists started to analyze locally generated high-frequency noise for their applicability in shallow-structure inversions (e.g., Draganov *et al.*, 2007; Picozzi *et al*., 2009; Behm *et al*., 2014; Tibuleac *et al.*, 2015). The use of local, high-frequency seismic noise in GF calculations, which is used to measure the wave velocity of the Earth medium, incurs new challenges. These local noises may not be ubiquitous. Their temporal and spectral characteristics may also change from time to time, and from place to place.

In this study, we calculate GFs using ambient seismic noise data recorded by a small geophone array installed at the Raft River geothermal field in southern Idaho. We measure Rayleigh-wave group velocities between geophones from the GFs and invert for 2D group-velocity maps at multiple frequencies for the area. These 2D models would be used to construct a low-resolution 3D velocity model to be used as the initial model for velocity inversions using active seismic data and microseismic data to develop a high-resolution velocity model.

2. DATA

A small, high-frequency geophone array has been installed at the Raft River geothermal field in the vicinity of an EGS well. Figure 1 shows the layout of the array. Also shown in the figure is the location of the EGS well. The geophone array is composed of eight stations. Four of the stations are surface stations whereas the rest are borehole stations installed at 91.44-m depth. The array covers an area of about 3-by-4 kilometers. The shortest inter-station distance is 942 m and the longest inter-station distance is 4630 m. Ground motion is continuously recorded by the array to monitor local seismicity and background seismic noise. The sampling rate of the data is 500 samples/s. We use the ambient seismic noise data recorded using the geophone array from October 2013 to July 2015 for our analysis. Figure 2 gives an example of seismic noise recorded by one of the geophones after its mean is removed. Figure 3 shows its spectrum, which is typical for all geophone locations. In addition to the broad spectral energy, there are several prominent spikes in the spectrum. These are possibly caused by the machinery that has been operating at the geothermal field, such as the power plant. Although

the geophones are three-component geophones, we only use vertical-component seismograms in our CC calculations. Our focus is on the fundamental-mode Rayleigh wave, which has the largest particle motion in the vertical direction. We may explore the use of other components in the future.

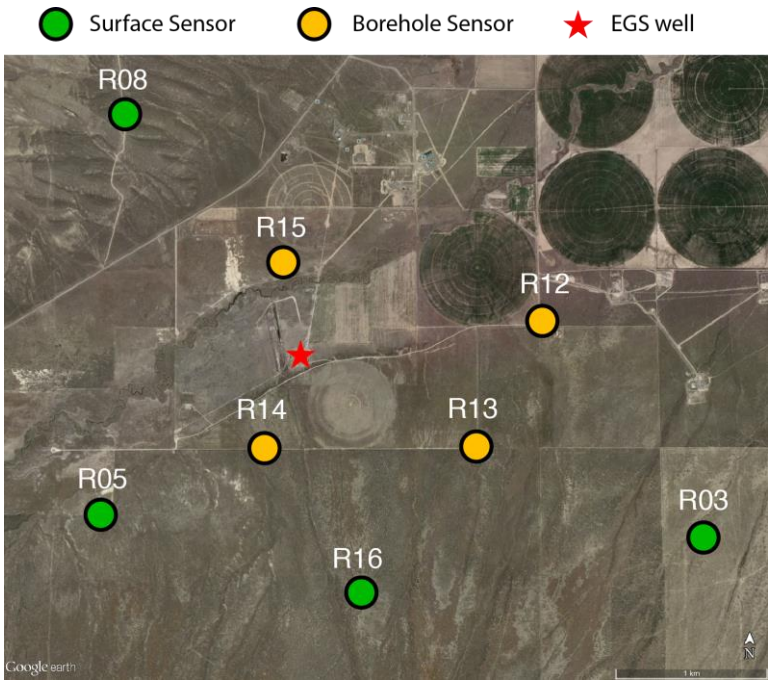

Figure 1: The layout of the geophone array at the Raft River geothermal field to record ambient seismic noise and microseismicity. Four sensors are installed at the surface whereas the other four sensors are borehole sensors at 91.44 m depth. Station IDs are marked above the stations. Red star indicates the location of a well for the EGS project at the geothermal field.

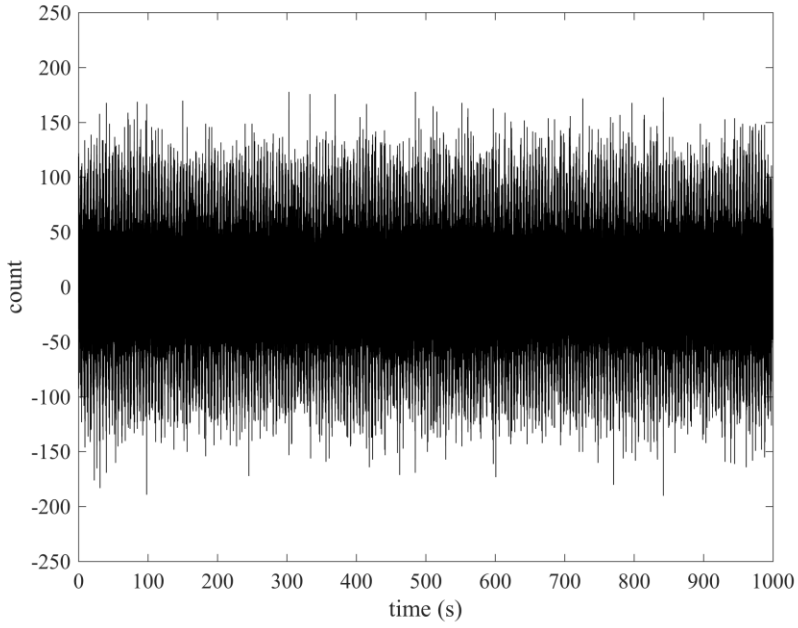

Figure 2: An example of ambient noise data recorded by one of the surface geophones after its mean is removed.

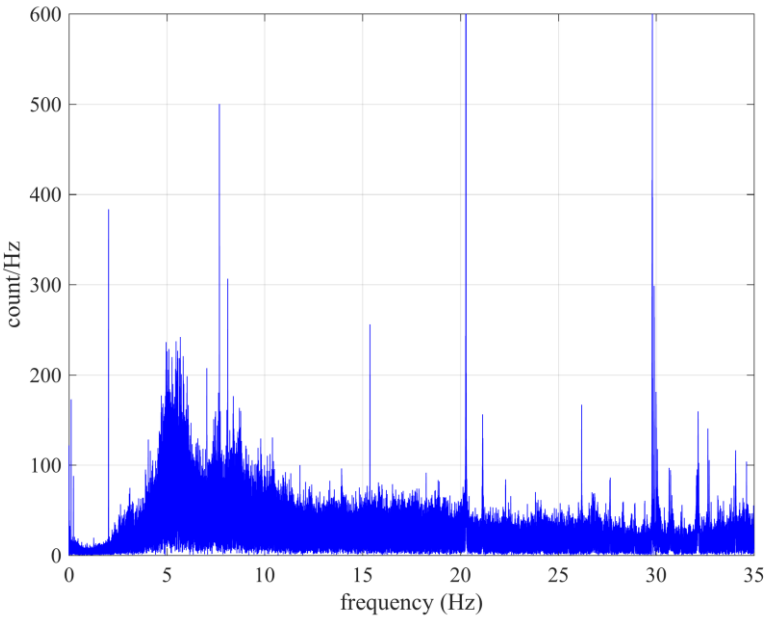

Figure 3: Amplitude spectrum of data shown in Figure 2. The spectrum is shown only up to 35 Hz, below which we can detect Rayleigh-wave energy.

3. CROSS-CORRELATION CALCULATION

We cross-correlate ambient seismic noise data recorded by two seismic stations at different locations to obtain the GF between the two stations as if one of the stations were the source. The GF contains all seismic phases including both body and surface waves. In most cases, however, surface waves dominate the GF. Oftentimes body waves are not apparent because of poor signal-to-noise ratios. The noise cross-correlation method has been widely used to derive large-scale velocity models for different parts of the world. Examples include Shapiro *et al.* (2005), Sabra *et al.* (2005), Yao *et al.* (2006) and Lin *et al.* (2007). Standard data processing procedures have also been developed (Bensen *et al*. 2007). In recent years, the CC method has been applied to small-scale problems to retrieve high-frequency surface waves that sample the shallow structure (Draganov *et al.*, 2007; Picozzi *et al*., 2009; Behm *et al*., 2014; Tibuleac *et al.*, 2015).

We follow the procedure of Lin *et al.* (2013) to process the noise data and to calculate CC. We first divide the continuous data into 30-min non-overlapping segments. For each segment, we rebalance the spectral content of the signal by spectral whitening. We then calculate the CC between all possible station pairs for each segment. To reduce the effect of transient signals such as earthquakes and instrument glitches, we divide the resulting CC by their maximum absolute amplitudes (Prieto *et al.*, 2011). Finally, we stack the calculated CC from all segments to obtain the final result. The length of our dataset is about 400 days. This is equivalent to ~19000 individual CC for each stacked CC.

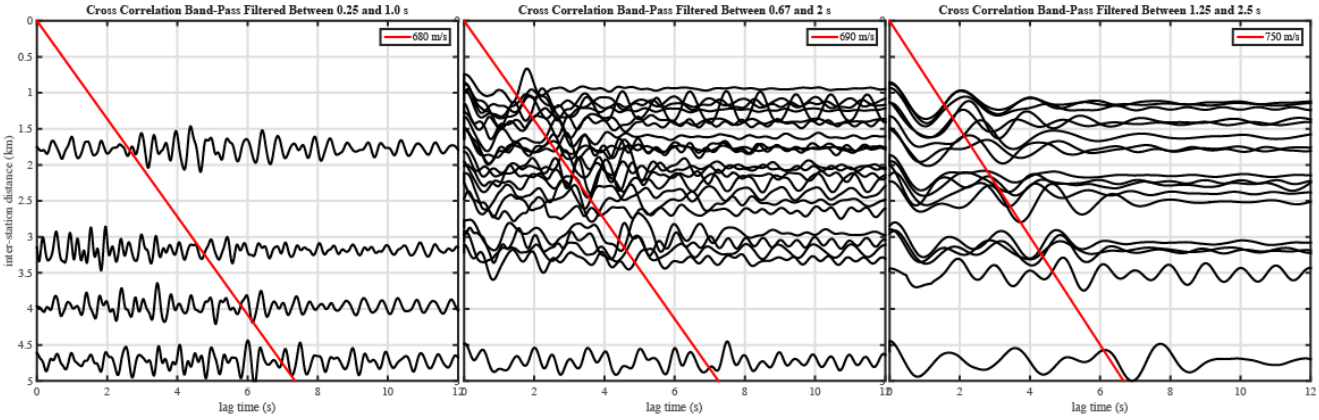

Figure 4: Cross correlations filtered for different frequency bands. Red lines mark the onset of the Rayleigh-wave signal. Their corresponding velocities are in the legend.

Although the CC has energy up to the Nyquist frequency of 250 Hz, discernible Rayleigh wave signal only appears in a more limited frequency range, in this case, between about 0.2 to 35 Hz. Figure 4 shows traces of CC filtered for selected frequency bands. Not all CC traces show clear Rayleigh wave signal even after filtering. Figure 4 only displays those traces where Rayleigh wave can be identified. The red line in each panel marks the onset of the Rayleigh wave. The move-out velocities, indicated in the legend, show an increasing velocity as the period increases, consistent with a normal dispersion behavior.

4. SURFACE-WAVE DISPERSION MEASUREMENT

Before we make surface-wave dispersion measurements from the GFs, we estimate the average surface-wave dispersion for the whole area covered by the geophone array. We use a frequency-wavenumber (f-k) analysis using continuous-wavelet transform (CWT) filters for the estimation. The average dispersion is then used as a guide to help pick the proper dispersion curve from the sometime noisy data.

We use the MFA technique to measure surface-wave dispersions. We first band-pass filter the CC using a frequency-domain Gaussian filter at multiple frequencies between 0.1 and 35 Hz. The filter is defined as

$$F(w) = e^{-a\frac{(w-w_0)^2}{w_0^2}}, \quad (1)$$

where ω is the angular frequency, ω_0 is the center angular frequency of the filter, and α is a scaling factor that is set to 1. After filtering, we plot the amplitude envelope of filtered CC as a function of period and group velocity, defined as distance/time. From the displayed image, we measure the surface-wave dispersion that corresponds to the maximum envelope amplitudes. Figure 5 illustrates how the surface-wave dispersion is measured.

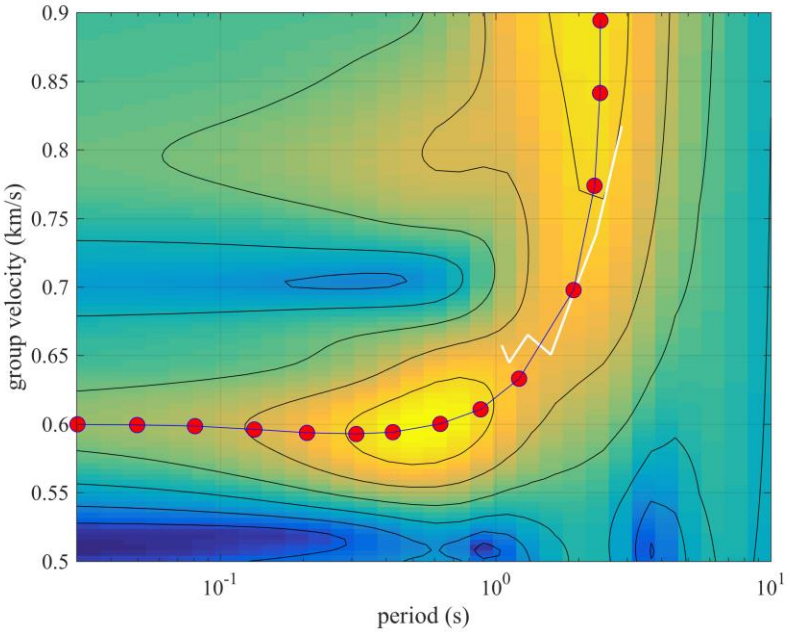

Figure 5: An example of how surface-wave dispersion is measured. Amplitude envelope of band-pass filtered CC versus group velocity is displayed at different periods. Surface-wave dispersion (group velocity versus period, red dots) is then traced along maximum envelope amplitudes. The white line shows the average dispersion of the study area from the f-k analysis.

If the noises sources are uniformly distributed in space, GF should appear on both positive and negative lag times of the CC. In most cases, however, the noise distribution is not uniform. As a result, the symmetry of the CC does not always exist. Clear GF could appear in either the positive lag-time or the negative lag-time portion of the CC, but not in both. In some cases, the stacking of positive and negative lag-time portions of the CC to create a symmetric CC would yield better GF. For this reason, we analyze positive lag-time, negative lag-time and symmetric CC at the same time and measure the surface-wave dispersion from the CC that show the clearest surface-wave signal. For example, the result shown in Figure 5 is from a symmetric CC.

5. SURFACE-WAVE VELOCITY MODEL INVERSION

We perform tomographic inversions using measured surface-wave slowness values to develop 2D surface-wave velocity maps at multiple frequencies for the study region. Measured slowness between stations *i* and *j* can be expressed as the accumulation of laterally varying slowness along the path:

$$s_{ij} = \frac{1}{\Delta_{ij}} \sum_{k=1}^{m} \sum_{p=1}^{n} s_p a_{kp} \Delta_k , \tag{2}$$

where s_p is discretized laterally varying slowness; a_{kp} is weighting coefficient; Δ_k is path segment length and Δ_{ij} is total path length. Combining slowness measurements for all paths, Eq. (2) becomes

$$\mathbf{d} = \mathbf{Gm}, \tag{3}$$

where $\mathbf{d}$ is the data vector containing all measured slowness s_{ij}, $\mathbf{m}$ is the model vector containing all s_p for the area, and $\mathbf{G}$ is the data kernel. We solve Eq. (3) for the slowness model $\mathbf{m}$ via a Bayesian least-squares inversion:

$$\mathbf{m} = \mathbf{m}_p + (\mathbf{G}^T \mathbf{C}_\mathbf{d}^{-1} \mathbf{G} + \mathbf{C}_{\mathbf{m}p}^{-1})^{-1} \mathbf{G}^T \mathbf{C}_\mathbf{d}^{-1} (\mathbf{d} - \mathbf{G}\mathbf{m}_p), \tag{4}$$

where $\mathbf{C_d}$ is the data covariance; $\mathbf{m}_p$ is the *a priori* model; and C_{mp} is its covariance (Tarantola, 1987; Menke, 1989). To conduct inversion using Eq. (4), we construct a constant *a priori* model by averaging measured slowness values. We select data and model covariance such that the resulting model has values that fall within a reasonable range and the model is reasonably smooth.

To show how the area is sampled with the measurements, Figure 6 plots the path coverage of measured slowness at 2 Hz. Because of the relatively sparse distribution of seismic stations, the spatial coverage is not so good. Nevertheless, we are able to invert for a model with the resolution on the order several hundred meters, fulfilling the goal of developing the low-resolution velocity model to be used as the initial model in multi-scale high-resolution velocity model inversions.

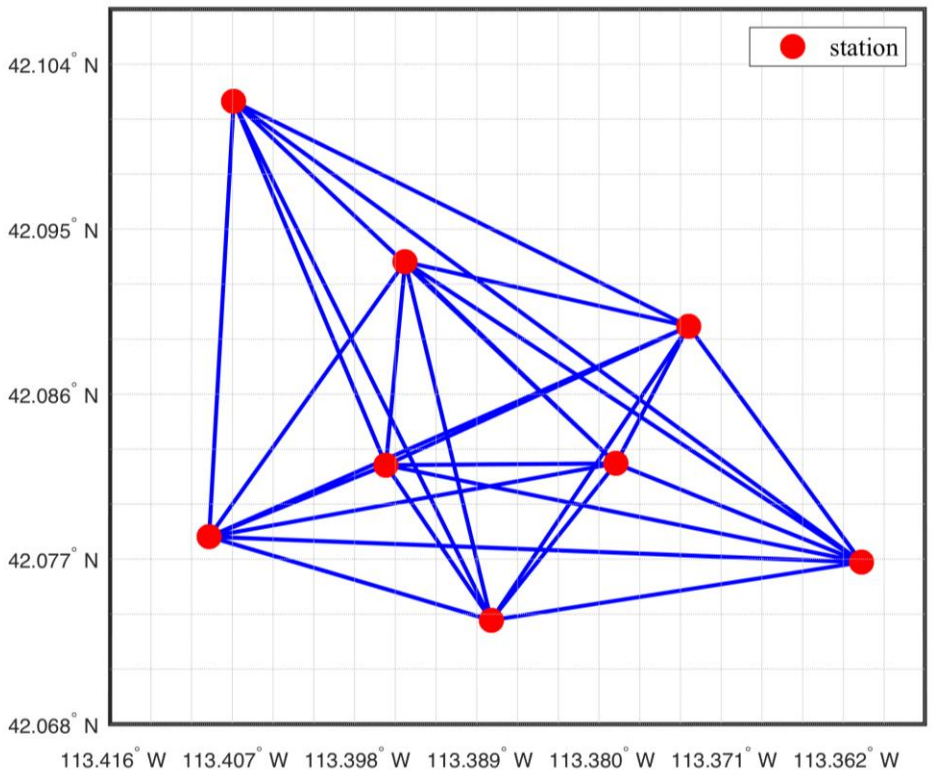

Figure 6. Path coverage of measured slowness at 2 Hz.

Using measured surface-wave slowness values, we invert for 2D slowness models for the study area at multiple frequencies. In Figure 7, we show selected results at 0.5, 0.67, 1.0 and 2.0 Hz as Rayleigh-wave group-velocity maps. Although the maps are displayed as cells, they are actually node based. Since no smoothing is applied during plotting, each node is plotted as a square with a constant velocity value.

Overall the velocity is low with a maximum velocity of 1.08 km/s and a minimum velocity of 0.55 km/s. One prominent feature of the models is a relatively high-velocity region in the middle of the study area. This feature is persistent at all frequencies. For the rest of the study area, the velocity variation is relatively small. In general, velocities increase as the frequency decreases. In areas without ray path coverage, the models do not have velocity values. The size of the model area correlates with the quality of the ray-path coverage. For example, larger model areas at high frequencies correspond to better ray-path coverage at those frequencies. Overall, the spatial extent

of the velocity model at all frequencies, which is dictated by the geophone array coverage, includes the key monitoring region of the EGS project, where the final high-resolution velocity model is to be developed.

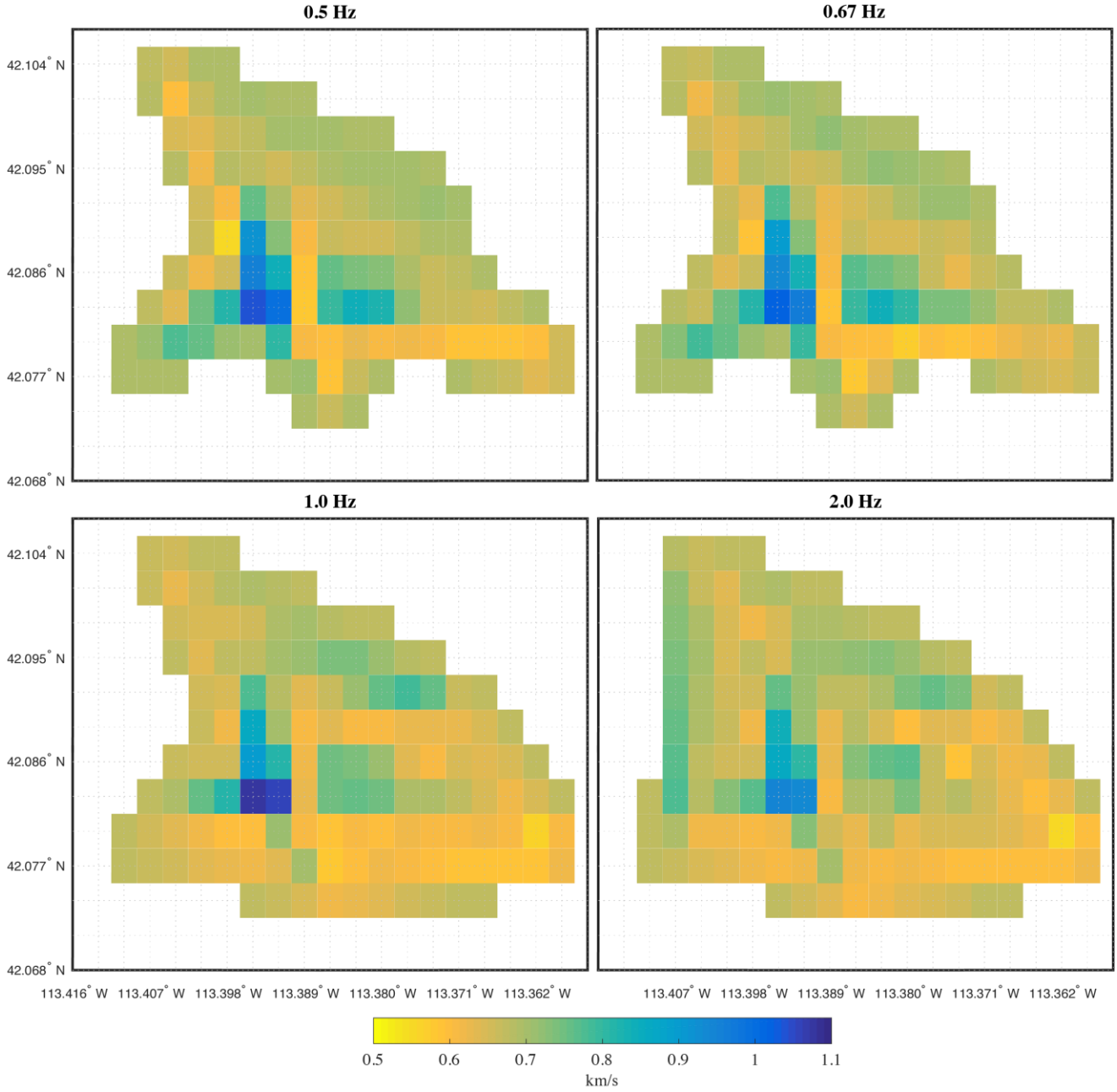

Figure 7: Rayleigh-wave group velocity models at 0.5, 0.67, 1.0 and 2.0 Hz obtained from ambient-seismic-noise based surface-wave dispersion measurements.

Figure 8 plots the data misfits from the final model prediction compared with those from the *a priori* constant model prediction at 0.5, 0.67, 1.0 and 2.0 Hz. It shows that the tomographic inversion reduces the misfit significantly. The overall misfit variance reduction is around 80%.

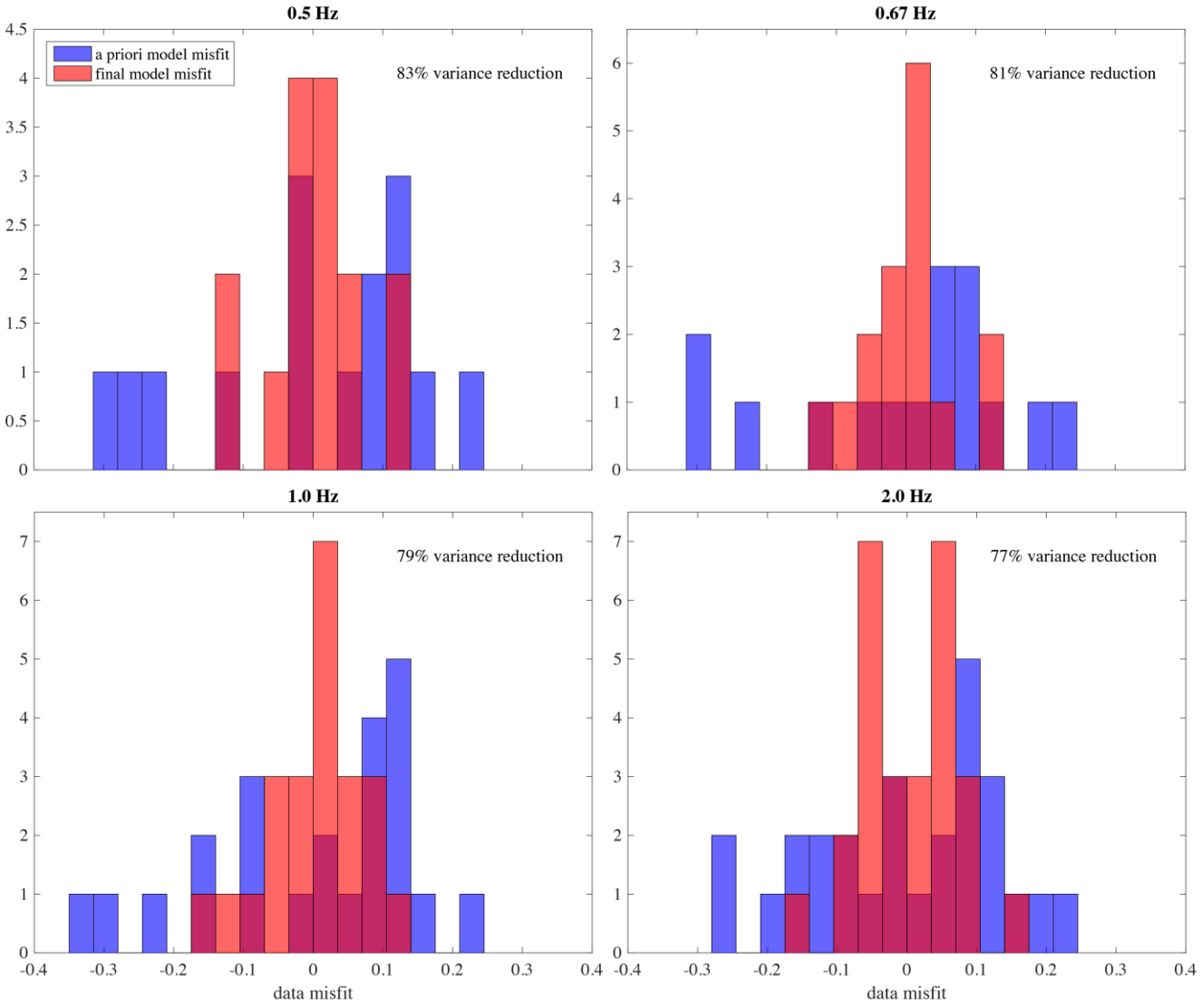

Figure 8: Comparison of data misfits between the constant *a priori* model prediction and the final tomographic model prediction at 0.5, 0.67, 1.0 and 2.0 Hz.

6. CONCLUSIONS

By cross-correlating ambient seismic noise recorded by a small geophone array at the Raft River geothermal field, we have extracted fundamental-mode Rayleigh-wave signals between station pairs. We have then measured surface-wave group velocities from the surface-wave signal using a multiple-filter analysis technique, used these velocity measurements to perform tomographic inversion, and obtained low-resolution 2D velocity models for the study area. Surface-wave group velocities of the models range from 0.55 km/s to 1.08 km/s. With the Bayesian tomographic inversion, we are able to reduce the variance of the data misfit from the initial constant model prediction by about 80%. These low-resolution velocity models would be used as initial models in a multi-scale approach to high-resolution 3D velocity model building for an EGS project at the Raft River geothermal field.

REFERENCES

Behm, M., Leahy, G. M., and Snieder, R.: Retrieval of Local Surface Wave Velocities from Trafic Noise – an Example from the La Barge Basin (Wyoming), *Geophys. Pros.*, **62**, (2014), 223-243, doi:10.1111/1365-2478.12080.

Bensen, G. D., Ritzwoller, M. H., Barmin, M. P., Levshin, A. L., Lin, F. –C., Moschetti, M. P., Shapiro, N. M., and Yang, Y.: Processing Seismic Ambient Noise Data to Obtain Reliable Broad-Band Surface Wave Dispersion Measurements, *Geophys. J. Int.*, **169**, (2007), 1239-1260.

Draganov, D., Wapenaar, K., Mulder, W., Singer, J., and Verdel, A.: Retrieval of Reflections from Seismic Background-Noise Measurements, *Geophys. Res. Lett.*, **34**, (2007), L04305, doi:10.1029/2006GL028735.

Lin, F. –C., Ritzwoller, M. H., Townend, J., Savage, M., and Bannister, S.: Ambient Noise Rayleigh Wave Tomography of New Zealand, *Geophys. J. Int.*, **170**, (2007), 649-666.

Lin, F. –C., Li, D., Clayton, R. W., and Hollis, D.: High-Resolution 3D Crustal Structure in Long Beach, California: Application of Ambient Noise Tomography on a Dense Seismic Array, *Geophysics*, **78**, (2013), Q45-Q56, doi:10.1190/GEO2012-0453.1.

Menke, W.: *Geophysical Data Analysis: Discrete Inverse Theory*, (1989), Academic, San Diego, California.

Picozzi, M., Parolai, S. Bindi, D., and Strollo, A.: Characterization of Shallow Geology by High-Frequency Seismic Noise Tomography, *Geophys. J. Int.*, **176**, (2009), 164-174, doi:10.1111/j.1365-246X.2008.03966.x.

Prieto, G. A., Denolle, M., Lawrence, J. F., and Beroza, G. C.: On the Amplitude Information Carried by Ambient Seismic Field: *Comptes Redus Geoscience*, **343**, (2011), 600-614, doi:10.1016/j.crte.2011.03.006.

Sabra, K. G., Gerstoft, P., Roux, P., Kuperman, W. A., and Feher, M. C.: Surface Wave Tomography from Microseisms in Southern California, *Geophys. Res. Lett.*, **32**, (2005), L14311, doi:10.1029/2005GL023115.

Shapiro, N. M., Campillo, M., Stehly, L., and Ritzwoller, M. H.: High-Resolution Surface-Wave Tomography from Ambient Seismic Noise, *Science*, **307**, (2005), 1615-1618.

Tarantola, A.: *Inverse Problem Theory*, (1987), Elsevier Science, New York.

Tibuleac, I. M., Iovenitti, J., Pullammanappallil, S., Ibser, F. H., von Seggern, D., Shaw, D., and McLahlan, H.: Development of a Low Cost Method to Estimate the Seismic Signature of a Geothermal Field from Ambient Seismic Noise Analysis, *Final Report*, DOE Geothermal Technologies Office (2015).

Yao, H., and van der Hilst, R. D.: Surface-Wave Array Tomography in SE Tibet from Ambient Seismic Noise and Two-Station Analysis: I – Phase Velocity Maps, *Geophys. J. Int.*, **166**, (2006), 732-744.